Numerical Modeling of Internal Tide Generation along the Hawaiian Ridge

S. K. KANG

Korea Ocean Research and Development Institute, Seoul, Korea

M. G. G. FOREMAN, W. R. CRAWFORD, AND J. Y. CHERNIAWSKY

Institute of Ocean Sciences, Department of Fisheries and Oceans, Sidney, British Columbia, Canada

(Manuscript received 8 October 1998, in final form 18 June 1999)

ABSTRACT

Internal M_2 tides near Hawaii are investigated with a two-dimensional, two-layer numerical model. It is seen that along the Hawaiian Ridge barotropic tidal energy is transformed into baroclinic internal tides that propagate in both northeast and southwest directions, as previously hypothesized. The internal tide for a certain beam is seen to propagate well over 1000 km. with an approximate decay scale of 1000 km. An asymmetric pattern in the baroclinic energy flux is observed to the north and south of the Hawaiian Ridge due to the spatially inhomogeneous baroclinic energy sources.

The surface manifestation of the M_2 internal tide in the model is compared with analysis results from TOPEX/Poseidon satellite altimetry. The baroclinic short-wave variation of a few centimeters amplitude, superposed on the barotropic surface amplitude, agrees well with the altimeter analyses. This, together with snapshots of the interfacial disturbance, allows the authors to sketch the propagation pattern of internal waves emanating northward and southward from the Hawaiian Ridge. Tidal current ellipses in the upper layer are dominated by the baroclinic internal tide with large spatial variability in their magnitude compared to the barotropic tidal ellipses.

The M_2 baroclinic energy flux is over 10 kW m^{-1} for the strongest energy beam propagating toward the northeast. Along the western Hawaiian Ridge about 3.8 GW of tidal power is converted from barotropic to baroclinic motion. The average northward or southward flux density for the first baroclinic mode is about 1.35 kW m^{-1} in the western Hawaiian Ridge. Also, if 2.7 kW m^{-1} (1.35 kW m^{-1} to each direction) is assumed for the whole 2000-km-long Hawaiian Ridge, a total of 5.4 GW is obtained. This value indicates that there is still a large uncertainty in the rate of barotropic to radiating baroclinic energy conversion along the Hawaiian Ridge.

1. Introduction

The existence of internal tides around the Hawaiian Ridge in the North Pacific has been recognized from various field observations (Noble et al. 1988; Chiswell 1994; Dushaw et al. 1995) and recently from the analysis of TOPEX/Poseidon satellite altimetry (Ray and Mitchum 1996). Using 9 months of moored current meter data above Horizon Guyot, a seamount located in the central Pacific near 19°N, 191°W, Noble et al. (1988) reported that the M_2 isotherm deflection amplitude was 20 m and the currents were two to three times larger than those predicted for this region by barotropic models. They suggested that these were predominantly due to an internal tide generated at the guyot. Using the hydrographic data obtained from monthly cruises collected as part of the World Ocean Circulation Experiment (WOCE), Chiswell (1994) found that the internal tides have peak-to-trough vertical displacements of up to 30 dbar at the Hawaiian Ocean Time Series (HOTS) site. Using the results from an acoustic experiment over the northern area of the Hawaiian Ridge, Dushaw et al. (1995) reported that the baroclinic tidal signals were consistent with a large-scale, phase-locked internal tide, apparently propagating northward over 2000 km from the Hawaiian Ridge. They mentioned that the amplitude, phase, and polarization of the first-mode M_2 baroclinic tidal displacement and current were consistent with a northward propagating internal tide and suggested that the internal tide is likely to be generated along the Hawaiian Ridge. In their analysis of TOPEX/Poseidon satellite altimetry, Ray and Mitchum (1996, 1997) showed that short-wavelength fluctuations in the ocean surface tide can be attributed to internal tides and that a significant fraction of the semidiurnal internal tide generated at the Hawaiian Ridge is evidently phase-locked to the astronomical potential and can modulate the amplitude of the surface tide by up to 5 cm. The increasing (decreasing) baroclinic phase lags, which they observed northward (southward) of the Hawaiian Ridge, confirm the Dushaw et al. (1995) hypothesis of generation along the ridge.

Corresponding author address: Dr. Sok Kuh Kang, Korea Ocean Research and Development Institute, Ansan, P.O. Box 29, Seoul 425-600, Korea.
E-mail: skkang@kordi.re.kr

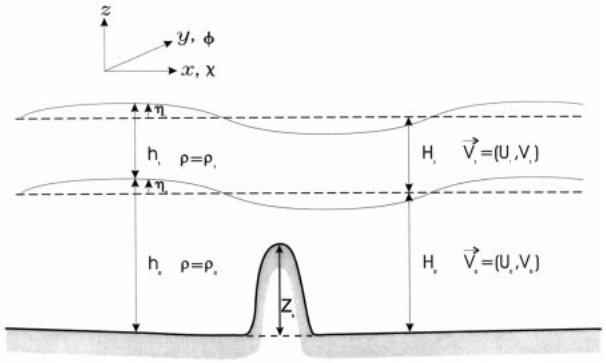

FIG. 1. Definition sketch for a two-layered, stratified flow.

Even though the evidence for the existence of internal tides around the Hawaiian Ridge is very strong, numerical modeling in the region, to our knowledge, has been restricted to the global barotropic tide (e.g., Schrama and Ray 1994; Le Provost et al. 1995). Various types of numerical models have been used to study internal tides around the world (e.g., Holloway 1996; Cummins and Oey 1997). These models can be classified into several groups according to the numerical method employed or the simplification of the governing equations.

A simple but useful treatment of the internal tide can be obtained with a layered model. A two-layer model can resolve the barotropic mode and the first baroclinic mode, while an additional second baroclinic mode can be resolved with a three-layer model. Pingree et al. (1983) and Serpette and Maze (1989) used simple two-layer models in their respective Celtic Sea and Bay of Biscay studies, while a three-layer nonlinear numerical model was developed by Willmott and Edwards (1987) for investigating tidally forced nonlinear internal wave generation over large-scale, one-dimensional (x–z), bottom topography. Their three-layer model was applied to Knight Inlet on the British Columbia coast and to the edge of the Armorican shelf in the Celtic Sea. In the Knight Inlet application, internal tides were generated over the sill top and propagated in both directions in the form of internal bores. Most numerical models have concentrated mainly on the continental shelf or slope regions rather than the underwater ridges. However, if the major axis of the tidal current is directed across a ridge, the cross-isobath energy fluxes may greatly exceed those at the continental slopes, where most of the tidal energy flux is generally directed parallel to the slope (Morozov 1995).

In this paper, numerical modeling of the generation, propagation, and surface manifestation of the internal tide confirms the hypothesis of Dushaw et al. (1995) and the results of Ray and Mitchum (1996) by showing that internal tides are generated by interaction of barotropic tides with the Hawaiian Ridge. The surface manifestation of the internal tide is also examined through a comparison between model results and TOPEX/Poseidon data. This manifestations has, to our knowledge, been rarely examined before, partly because its magnitude is of the order $\Delta\rho/\rho_0$ times η_0 (LeBlond and Mysak 1978; Apel 1987), where $\Delta\rho$, ρ_0, and η_0 denote the density difference between upper and lower layers, the density of lower layer, and the interfacial disturbance, respectively. Consequently, an interfacial height amplitude of 10 $\sim$ 20 m leads to a surface manifestation of only a few centimeters, thus causing detection difficulties in the field observations.

A global M_2 ocean dissipation of 2.4 TW (TW: terawatts) seems to be finally well established (Munk 1997; Ray and Mitchum 1997; Munk and Wunsch 1998). The analysis of TOPEX/Poseidon altimetry has reopened the problem of how tidal dissipation is to be allocated (Munk 1997), and Munk and Wunsch (1998) have presented an impressive budget of the tidal energy flux. Egbert et al. (1994) has applied inverse methods to estimate 1.8 TW of M_2 dissipation for a bottom boundary layer. The remaining 0.6 TW (M_2) must then be lost over deep sea ridges and seamounts. By measuring the surface manifestation of internal tides, Ray and Mitchum (1997) estimated a transfer of 15 GW of first mode, baroclinic M_2 tide along the Hawaiian Ridge, while Morozov (1995) obtained 8 GW based upon the Baines (1982) model. Taking 4 kW m^{-1}, as a representative transfer rate, Munk (1997) has estimated a global transfer of 0.2 TW for 50 000 km of global submarine ridges (equivalent to 14 Hawaiian Ridges). Munk and Wunsch (1998) have suggested that the remaining power could either be in the form of trapped baroclinic tidal energy or be associated with a direct conversion to turbulent dissipation. Given this interest in tidal dissipation, the aim of this paper is to study the energy conversion from a barotropic tide into a radiating baroclinic internal tide along the western Hawaiian Ridge, a reference region where relatively large differences exist between different estimates (8–15 GW) of the generated baroclinic energy.

TOPEX/Poseidon track 125 crosses the Hawaiian Ridge from SW to NE through the French Frigate Shoals (Fig. 2). The Ray and Mitchum (1996) spectral analysis of the M_2 wavetrains along track 125 revealed a dominant wavelength of approximately 150 $\pm$ 10 km. Dushaw et al. (1995) estimated the first baroclinic wavelength to be 156 km, based upon CTD surveys at 40°N, which is the only mode that could be observed in this experiment. Since it is well known that the interaction of barotropic tidal forcing with bottom topography and stratification is the main factor for internal tide generation, it follows that the internal tide and its surface manifestation can be studied successfully in the North Pacific by considering only the barotropic and first baroclinic mode. Therefore, in our Hawaiian Ridge experiments, a two-layer numerical model is employed to resolve the barotropic and first baroclinic modes of the tide. However, we acknowledge that two-layer modeling

is only one of several possible approaches for investigating internal tide generation.

2. A two-layer numerical model

a. Model formulation

A two-layer, stratified, nearly horizontal flow is considered according to the definition sketch shown in Fig. 1. The governing equations for the two-layer flow are described under the spherical polar coordinate system. For a two-layered flow, the usual depth-averaged two-dimensional equations for shallow water waves can be alternatively represented in terms of layer-integrated velocities for each layer. The momentum and continuity equations of the upper and lower layers, without surface wind stress, are as follows.

Upper layer:

$$\frac{\partial U_1}{\partial t} + \frac{1}{R\cos\phi}\frac{\partial}{\partial\chi}\left(\frac{U_1^2}{h_1}\right) + \frac{1}{R}\frac{\partial}{\partial\phi}\left(\frac{U_1V_1}{h_1}\right) = -\frac{gh_1}{R\cos\phi}\frac{\partial}{\partial\chi}(h_1 + h_0 + Z_b) + 2\omega\sin\phi V_1 - \frac{K_i}{\Delta z}\left(\frac{U_1}{h_1} - \frac{U_0}{h_0}\right) + \frac{U_1V_1\tan\phi}{Rh_1} + F_\chi \tag{1}$$

$$\frac{\partial V_1}{\partial t} + \frac{1}{R\cos\phi}\frac{\partial}{\partial\chi}\left(\frac{U_1V_1}{h_1}\right) + \frac{1}{R}\frac{\partial}{\partial\phi}\left(\frac{V_1^2}{h_1}\right) = -\frac{gh_1}{R}\frac{\partial}{\partial\phi}(h_1 + h_0 + Z_b) - 2\omega\sin\phi U_1 - \frac{K_i}{\Delta z}\left(\frac{V_1}{h_1} - \frac{V_0}{h_0}\right) + \frac{V_1^2\tan\phi}{Rh_1} + F_\phi \tag{2}$$

$$R\cos\phi\frac{\partial h_1}{\partial t} + \frac{\partial U_1}{\partial\chi} + \frac{\partial(V_1\cos\phi)}{\partial\phi} = 0 \tag{3}$$

Lower layer:

$$\frac{\partial U_0}{\partial t} + \frac{1}{R\cos\phi}\frac{\partial}{\partial\chi}\left(\frac{U_0^2}{h_0}\right) + \frac{1}{R}\frac{\partial}{\partial\phi}\left(\frac{U_0V_0}{h_0}\right) = -\frac{gh_0}{R\cos\phi}\frac{\partial}{\partial\chi}(\lambda h_1 + h_0 + Z_b) + 2\omega\sin\phi V_0 - \frac{K_i}{\Delta z}\left(\frac{U_1}{h_1} - \frac{U_0}{h_0}\right) - \frac{K_b}{h_0}\sqrt{U_0^2 + V_0^2}U_0 + \frac{U_0V_0\tan\phi}{Rh_0} + F_\chi \tag{4}$$

$$\frac{\partial V_0}{\partial t} + \frac{1}{R\cos\phi}\frac{\partial}{\partial\chi}\left(\frac{U_0V_0}{h_0}\right) + \frac{1}{R}\frac{\partial}{\partial\phi}\left(\frac{V_0^2}{h_0}\right) = -\frac{gh_0}{R}\frac{\partial}{\partial\phi}(\lambda h_1 + h_0 + Z_b) - 2\omega\sin\phi U_0 - \frac{K_i}{\Delta z}\left(\frac{V_1}{h_1} - \frac{V_0}{h_0}\right) - \frac{K_b}{h_0}\sqrt{U_0^2 + V_0^2}V_0 + \frac{V_0^2\tan\phi}{Rh_0} + F_\phi \tag{5}$$

$$R\cos\phi\frac{\partial h_0}{\partial t} + \frac{\partial U_0}{\partial\chi} + \frac{\partial(V_0\cos\phi)}{\partial\phi} = 0, \tag{6}$$

where χ is longitude, ϕ is latitude, Z_b is bottom topography (Fig. 1), h_0 ($=H_0 + \eta_0$) is total water depth of the lower layer, h_1 ($=H_1 + \eta_1$) is total water depth of the upper layer, $\Delta z = 0.5(h_0 + h_1)$, U_1 (U_0) is mass flux of the upper (lower) layer in χ, V_1 (V_0) is mass flux of the upper (lower) layer in ϕ, R is radius of the earth, $\lambda = \rho_1/\rho_0$, K_b is the bottom friction coefficient, K_i is the interfacial shear stress coefficient, g is gravity acceleration, and F unresolved processes. Also H_0, η_0, H_1, and η_1 are the thickness of mean lower layer, the disturbance of lower layer, the thickness of mean upper layer, and the surface disturbance of upper layer, respectively, as shown in Fig. 1.

The full set of nonlinear equations is solved with an extension of the one-dimensional two-layer modeling scheme (Abbott 1979; Hodgins 1979; S. K. Kang 1986, unpublished manuscript) and a depth-averaged two-dimensional modeling method (Abbott et al. 1981; Kang et al. 1998) (see appendix A for additional details). Four component equations are solved in each directional sweep. That is the continuity and momentum equations for the upper and lower layers in the χ coordinate are

solved simultaneously, with dynamical linking and without resorting to the separation of variables or modes that was used, for example, in Serpette and Maze (1989). This strategy of simultaneously computing each variable is more efficient than mode splitting techniques for obtaining the instantaneous surface response to interfacial disturbances.

The bottom friction term for the lower layer has been expressed in quadratic friction form, following the general applicability of the quadratic friction law for the semidiurnal tide modeling (e.g., Pingree and Griffiths 1987), while the interfacial stress is assumed to vary linearly with the velocity difference between the two layers. This was found to work reasonably well for the exchange flow tests done in previous works (e.g., Hodgins 1979; S. K. Kang 1986).

The momentum diffusion term was considered in terms of a subgrid-scale modeling technique since momentum diffusion effects induced by the subgrid term are often larger than dispersion effects. All motions induced by small-scale processes, not directly resolved by the model grid (subgrid scale), are parameterized in terms of horizontal diffusion processes. The terms F_χ and F_ϕ represent these unresolved processes and can be written as

$$F_\chi \simeq \frac{\partial}{R\cos\phi\partial\chi}\left(2A_M\frac{\partial u_{0,1}}{R\cos\phi\partial\chi}\right) + \frac{\partial}{R\partial\phi}\left[A_M\left(\frac{\partial u_{0,1}}{R\partial\phi}+\frac{\partial v_{0,1}}{R\cos\phi\partial\chi}\right)\right] \quad (7a)$$

$$F_\phi \simeq \frac{\partial}{R\partial\phi}\left(2A_M\frac{\partial v_{0,1}}{R\partial\phi}\right) + \frac{\partial}{R\cos\phi\partial\chi}\left[A_M\left(\frac{\partial u_{0,1}}{R\partial\phi}+\frac{\partial v_{0,1}}{R\cos\phi\partial\chi}\right)\right], \quad (7b)$$

where $(u_{0,1}, v_{0,1})$ are χ and ϕ velocity components for lower (subscript 0) and upper (subscript 1) layers. With constant C_s, A_M is defined as follows.

$$A_M = C_s\Delta\chi\Delta\phi\left[\left(\frac{\partial u_{0,1}}{R\cos\phi\partial\chi}\right)^2+\frac{1}{2}\left(\frac{\partial v_{0,1}}{R\cos\phi\partial\chi}+\frac{\partial u_{0,1}}{R\partial\phi}\right)^2+\left(\frac{\partial v_{0,1}}{R\partial\phi}\right)^2\right]^{1/2}, \quad (7c)$$

where C_s is a constant, while $\Delta\chi$ and $\Delta\phi$ denote the grid interval in the χ and ϕ directions. For the coefficient of subgrid-scale stress we used the Smagorinsky (1963) diffusivity concept. The technique of subgrid-scale stress modeling is described in detail by Abbott and Basco (1989) and the method was successfully employed in the large-scale tidal modeling of Kang et al. (1998).

b. Computation and experiments

The initial and boundary conditions required for the solution of Eqs. (1) to (6) are described as follows. At $t = 0$, the values of

$$\eta_0 = \eta_1 = U_{0,1}(\chi, \phi, t) = V_{0,1}(\chi, \phi, t) = 0$$

are specified at all points. The initial thickness of the upper layer was set to $h_1 = 300$, 400, 500, or 1000 m. The model boundary is open on all sides and the boundary values were specified from an update of the Schrama and Ray (1994) global barotropic M_2 tide. These open boundary elevations are prescribed for a tide according to the expression;

$$\eta_0(t) = A\cos(\omega t - G), \quad (8)$$

where A is the tidal amplitude and G the Greenwich phase lag of the M_2 tide. The boundary elevation was defined as a variation of the interfacial surface while keeping the thickness of upper layer constant as 300, 400, 500, or 1000 m. Since the propagation speed of a surface gravitation wave is about 100 times faster than the internal wave speed,

$$\left\{\frac{\Delta\rho}{\rho_0}g\frac{H_0H_1}{(H_0+H_1)(1-f^2/\omega^2)}\right\}^{1/2}.$$

the response of an internal wave to the barotropic tidal wave traveling over the submarine ridge can be investigated.

Grid resolution is $\frac{1}{10}^\circ$ in latitude by $\frac{1}{10}^\circ$ in longitude. Thus, resolving a 150-km wavelength requires about 14 grid cells. The model domain is 10°–40°N and 180°–160°W and the total number of grid cells is 60 000. Bathymetry was obtained from interpolation of the ETOPO5 dataset. Depth contours are shown in Fig. 2, with a contour interval of 200 m for depths less than 1000 m. The TOPEX/Poseidon tracks are also shown. Minimum water depth was set in the model to be 400 m, 500 m, 600 m, or 1000 m in respective experiments. Maximum depth is about 7100 m. The time step used is 87.0 s.

The bottom friction coefficient was chosen to be $K_b = 0.0025$. In contrast to the relatively well-known K_b, the magnitude of the interfacial stress coefficient (K_i) is not well known. Given the Hodgins (1977) reasonable results with exchange flow tests, we used $K_i = 0.0015$ in most of the cases (Table 1). A value of $K_i = 0.0025$ was also used for comparison. The Smagorinsky eddy viscosity model was extended to the present two-layer model and the empirical constant of Eq. (7c) was chosen as $C_s = 0.3$ for each layer. This yields different viscosity coefficients. A_M, for each layer. Here $C_s = 0.3$ is a little larger than the value ($C_s \sim 0.2$) used by Deardorff (1971) in the three-dimensional study. This value was found to be proper for depth-averaged modeling (Kang et al. 1998).

Ray and Mitchum (1997) employed measurements from the HOTS experimental site (Tupas et al. 1995;

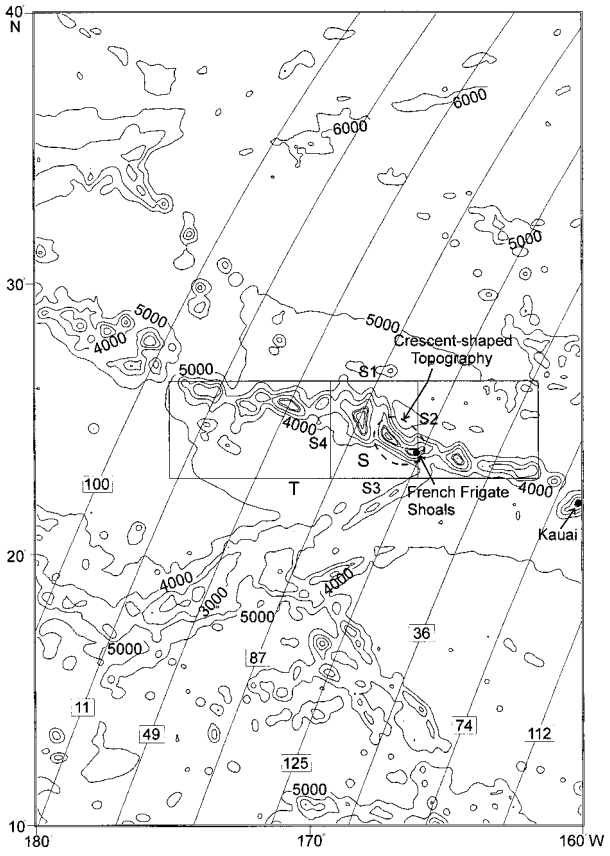

FIG. 2. Model domain for the western Hawaiian Ridge covering 180°–160°W in longitude and 10°–40°N in latitude. The depth contour interval is 200 m for depths less than 1000 m. The solid lines running from northeast to southwest, denote the tracks of the TOPEX/Poseidon satellite. S1–S4 are the sections across which energy flux values are calculated. Locations of the French Frigate Shoals and Kauai Island are marked as dark circles. Crescent-shaped bottom topography region is marked by a dashed line.

Karl and Lukas 1996) to estimate density and layer thickness for a simple analytical two-layer model. We adopt their values as parameters for our experimental cases. Specifically, they estimated the upper- and lower-layer densities $\rho_{1,0}$ to be 1024.7 and 1027.7 kg m^{-3} and the upper-layer thickness H_1 to be 300 m. Although the permanent thermocline depth is known to vary with latitude (Pickard 1979), this layer thickness is in rough agreement with the commonly chosen value of H_1 = 400 m (e.g., Gill 1982, section 6.3). However, a modal decomposition yields approximately 1000 m for the depth of maximum vertical velocity of the first mode and near 300 m for the second mode (P. Cummins 1999, personal communication). In order to estimate model response for the case H_1 = 1000 m, an additional run (RUN5) was also carried out.

Considering the extent of the model region, sensitivity to the choice of H_1 was investigated using the first three experiments listed in Table 1. The case without advection and diffusion was examined for H_1 = 400 m.

TABLE 1. Experimental cases in this study.

Experiment	H_1 (m)	$\Delta\rho/\rho_o$	K_i	Advection term (AT)
RUN1	300	0.0029	0.0015	Yes
RUN2	400	0.0029	0.0015	Yes
RUN3	500	0.0029	0.0015	Yes
RUN4	400	0.0029	0.0015	No
RUN5	1000	0.0019	0.0015	Yes
RUN6	400	0.0029	0.0025	Yes

The magnitude of the interfacial stress coefficient K_i was set to 0.0015 for most of cases. The value K_i = 0.0025 was also tested (RUN6).

Continuous model runs were carried out over nine M_2 tidal cycles. A FFT analysis over the ninth cycle was used to calculate amplitudes and phase lags of the M_2 tide. Snapshots of the interfacial variation for the first, third, seventh and ninth tidal cycle were also stored (and shown in Figs. 5a–d) in order to investigate the propagation pattern of the internal waves. The model run was stopped at the end of cycle 9 to avoid the reflection of internal waves from boundaries.

3. Results: Barotropic and baroclinic responses

Differences between the H_1 = 300-m, 400-m, and 500-m model results were not significant in the sense that the broadscale features of the internal tide looked similar. However, the magnitude of tidal oscillation did show some differences between experiments. The model response to different upper-layer thickness was evaluated by comparing the surface manifestation of the internal tide to TOPEX/Poseidon observations (see section 3b). The experiment (RUN4) without advection and diffusion terms did not show a remarkable difference from the nonlinear case (RUN2). This suggests that nonlinear effects are limited in the set up and propagation of internal waves. With larger interfacial coefficient (RUN6) the baroclinic surface disturbance along track 125 is seen to be reduced by about 35%, compared to RUN2. The amplitude appears smaller especially over the northern region. Since the RUN2 simulation has provided a better agreement with observations, the subsequent discussion will be mainly for the case of RUN2, in which H_1 = 400 m.

a. Surface and interfacial disturbances

The computed M_2 surface elevation amplitudes are presented in Fig. 3, while the comparable Schrama and Ray (1994) values are shown in Fig. 4. (The computed surface elevation phases were not presented due to complicated features arising from a superposition of barotropic and baroclinic effects.) The barotropic M_2 tide propagates from northeast to southwest. An amphidromic point exists outside the model region, near 30°N, 140°W (Irish et al. 1971; Ray and Mitchum 1997). The

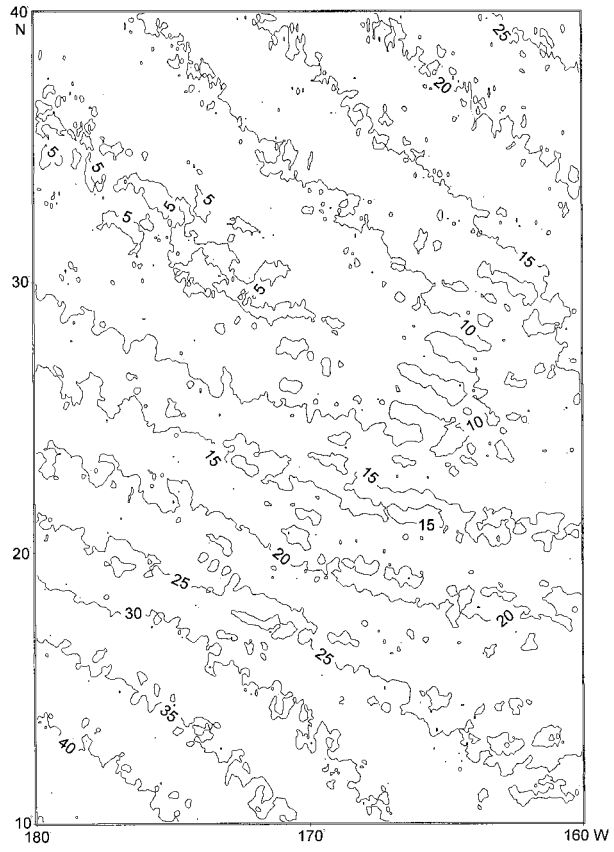

FIG. 3. Computed coamplitude lines (cm) of the M_2 tide. The irregular contour pattern is due to the surface manifestation of the internal tide.

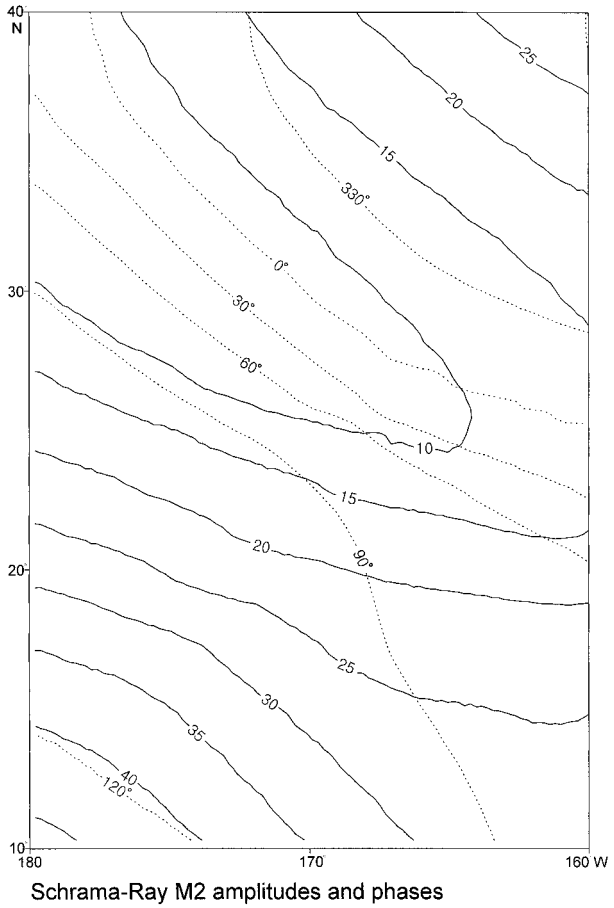

Schrama-Ray M2 amplitudes and phases

FIG. 4. Computed tidal chart of the semidiurnal M_2 constituent from Schrama and Ray (1986). Solid and dotted lines denote the coamplitude (cm) and cophase (degree) lines, respectively. When smoothed, coamplitude contours appear comparable to those in Fig. 3.

general patterns in the two tidal charts agree well, implying that the barotropic surface elevation has been simulated reasonably well with the present two-layer model. The general agreement between large-scale variations in the computed and observed barotropic tidal amplitude is again clear from a comparison in Fig. 6, in which short-scale baroclinic waves are superposed on large-scale barotropic waves. Careful inspection shows that short-scale disturbances in the amplitude and phase lag are present in the two-layer results, as shown, for example, in the 10 cm co-amplitude line of Fig. 3. A detailed description of this disturbance is given in section 3b.

The interfacial disturbance for the first, third, seventh, and ninth tidal periods are presented in Figs. 5a, 5b, 5c, and 5d, respectively. The slowly curving lines in Figs. 5a–d denote TOPEX/Poseidon satellite tracks. After one tidal cycle (Fig. 5a), an interfacial disturbance amplitude of up to nearly 20 m is generated around the Hawaiian Ridge. Since a baroclinic signal that originated at the outer boundary could not have reached the ridge by this time, the driving force must be the barotropic tide at the Hawaiian Ridge (Fig. 5a). Figures 5a–d show how the internal waves, generated along the Hawaiian Ridge, propagate mainly toward the northeast and southwest. (In section 3d, this is also discussed in terms of the baroclinic energy flux.) The wavelength of the internal wave is about 150 km, virtually the same as the Ray and Mitchum (1996) value.

Obviously, the internal tide is generated from multiple sources along the ridge. It propagates in a horizontal beamlike pattern and has an interesting interference feature. This purely horizontal beamlike pattern differs from the customary characteristic paths of internal tide that propagate vertically, as well as horizontally, as beams. Due to this horizontal beamlike pattern, it is difficult to determine a precise *e*-folding decay distance of the internal tide from amplitude variations along the TOPEX/Poseidon tracks. Although Ray and Mitchum (1996) found about a 300-km decay distance in some tracks, Fig. 5d, along with Fig. 6a, suggest that the internal tide propagates well over 1000 km and has an approximate 1000-km decay scale. This compares well with the description that, for a reasonable range of values for the eddy viscosity, long internal tides (wavelength of about 200 km) will propagate over distances of 2000 km or more (LeBlond 1966). Using a large

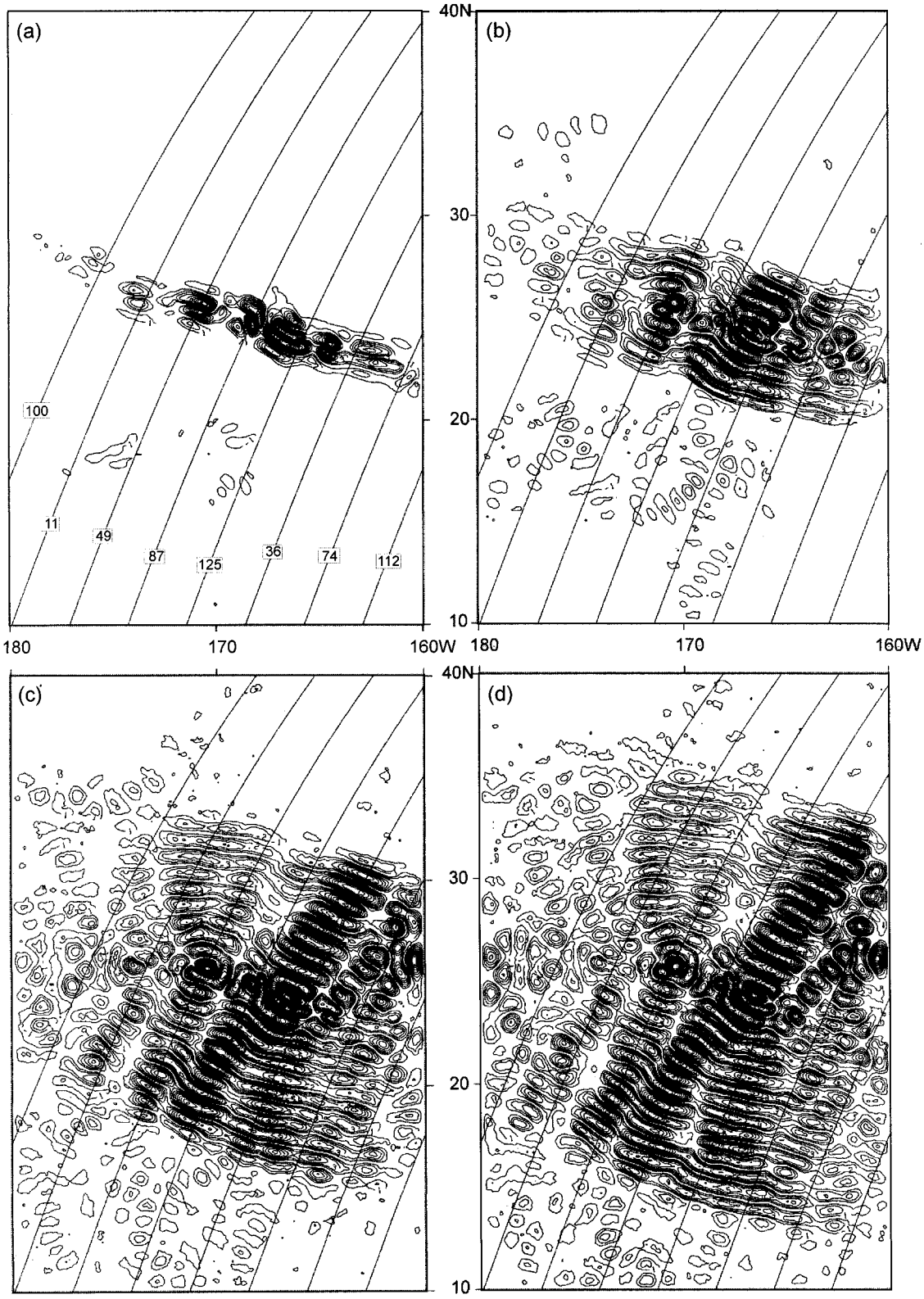

FIG. 5. Instantaneous height (m) of the interfacial disturbance after (a) 1, (b) 3, (c) 7, and (d) 9 cycles of computation for the M_2 tide. Internal tidal waves in (a) start to propagate in northeast and southwest directions from the Hawaiian Ridge, while the waves in (d) have propagated farther than 1000 km in each direction.

acoustical array located midway between Puerto Rico and Bermuda in the Atlantic, Dushaw and Worcester (1998) estimated the decay scale for the diurnal component to be about 2000 km.

Careful inspection of the propagation pattern along satellite tracks 87 and 125 (e.g., Fig. 5d) reveals an asymmetry between southwest and northeast propagation patterns. This is described in some detail in section 3d. It is also seen that the magnitude of the internal tidal amplitude is not uniform along all of the Hawaiian Ridge. This spatial nonuniformity could be caused by the different generation intensity from multiple sources, as well as by interference between the horizontal rays. The region that shows maximum power of internal tide generation is marked **S** in Figs. 2 and 11. The maximum amplitude in the internal tide appears between tracks 87 and 125.

b. Comparison of surface manifestation with TOPEX/Poseidon data

The propagation of the internal tide along the permanent thermocline creates a corresponding surface disturbance, as revealed by the Ray and Mitchum (1996) TOPEX/Poseidon analysis. Comparison between model (RUN2) and observed (TOPEX/Poseidon) M_2 amplitudes along four satellite tracks is shown in Fig. 6 [The analysis of TOPEX/Poseidon data is described in Cherniawsky et al. (1999, manuscript submitted to *J. Atmos. Oceanic Technol.*).]

As expected from the comparison between Figs. 3 and 4, the agreement in amplitudes at long wavelengths also indicates that the barotropic tide has been simulated reasonably well. The model results also show short wavelength oscillations in the amplitudes in Fig. 6. These oscillations compare well with the observed TOPEX/Poseidon values in both their magnitude and wavelengths. Specifically, a spectral analysis of the computed and observed oscillations along track 125 reveals the same peak at approximate wavelengths of 150 km. This is in close agreement with the wavelength observed by Ray and Mitchum (1996). The wavelength of the internal tide can also be analytically determined as $(g'H_1)^{1/2}T \approx 150$ km, for $h_1 \ll h_0$, where T is tidal period and reduced gravity $g' = (\rho_0 - \rho_1)g/\rho_0$ is calculated using layer densities from RUN2.

The computed M_2 amplitude of the 150-km wave along track 125 is larger than in the observations by about 15%. Spectral analysis also indicates that the computed baroclinic oscillation of short wavelength leads the observed wave by about 25° along track 125. Such a pattern of phase lags is also visible in Fig. 6. Ray and Mitchum (1996) interpreted these oscillations as the surface manifestation of phase-locked internal tides propagating off various topographic features, primarily the Hawaiian Ridge. The interface variations shown in Fig. 5, as well as their phase progression (not shown here), suggest that the internal tide is generated along the Hawaiian Ridge and propagates toward the northeast and southwest.

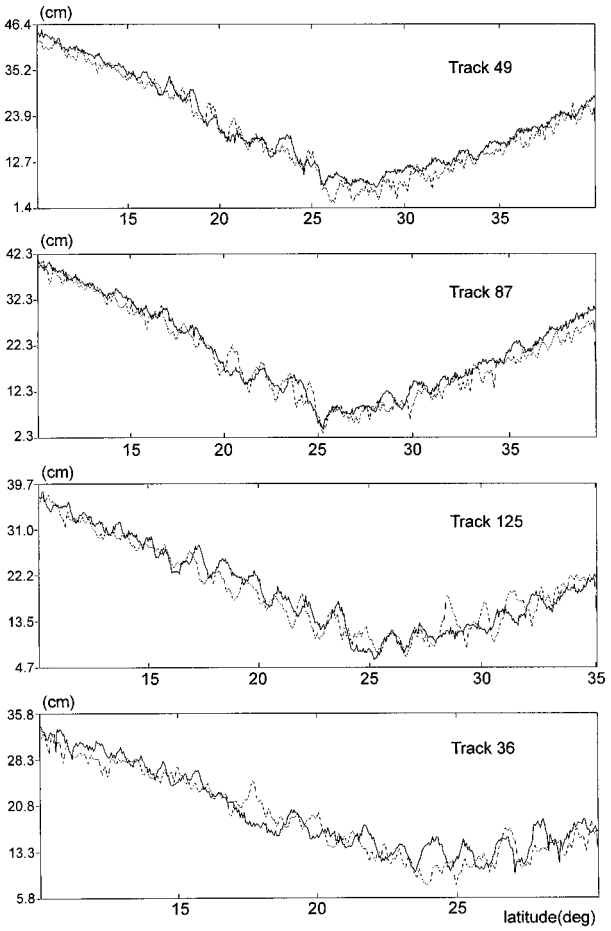

FIG. 6. Observed M_2 tidal amplitude (solid line) from the analysis of TOPEX/Poseidon data and calculated M_2 tidal amplitude (dotted line) from the two-layer model, with 400-m thickness of the upper layer and 6-min grid resolution (RUN2). Locations of tracks 49, 87, 125, 36 are shown in Fig. 2.

Figures 7a–d present a comparison along track 125 between observations and results from model runs 1, 3, 5, and 4. Spectral analyses of computed results of runs 1, 3, 5, and 4 reveal peaks at wavelengths of 137, 175, 189, and 167 km, respectively. The ratios of computed to observed elevation amplitude at each peak wavelength are 0.91, 1.11, 1.22, and 1.20, respectively. Less agreement between RUN4 and RUN2 appears in spite of a general similarity between the two experiments. The peak at a slightly longer wavelength (RUN4) may be due to the different horizontal beam propagation characteristics, arising from neglecting internal tide advection effects by barotropic currents, or nonlinear interactions between internal tide beams. In general, our comparison between model results and altimeter observations indicates that the North Pacific Ocean is modeled best with an upper-layer thickness of $H_1 = 400$ m

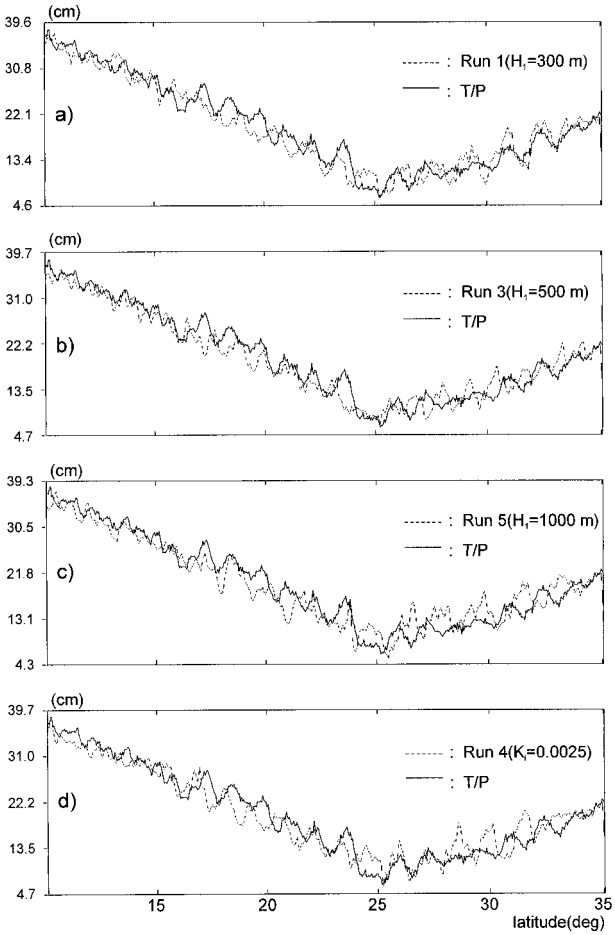

FIG. 7. Observed M_2 tidal amplitude (solid line) from the analysis of TOPEX/Poseidon data and calculated M_2 amplitude (dotted line) along track 125 for (a) RUN1, (b) RUN3, (c) RUN5, and (d) RUN4.

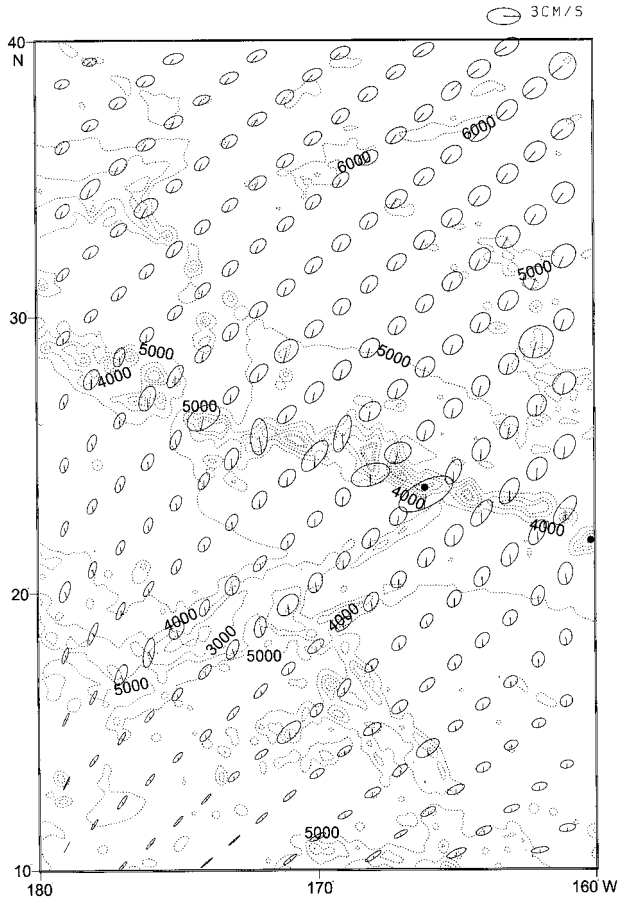

FIG. 8. The M_2 barotropic current ellipses from RUN2 with an upper layer thickness of 400 m. Note that the current speeds are about 2–3 cm s^{-1}, with slightly stronger speeds at ridge sites. Every 230th ellipse is shown. The same intervals between vectors or ellipses are shown in Figs. 9 and 10. Dotted depth contours are in meters, also shown in the following figures.

and with advection terms, as represented by RUN2 (see Fig. 6).

It is obvious that the internal wave will have both in-phase or out-of-phase contributions with the background barotropic tidal waves, resulting in fluctuating amplitudes of the barotropic (vertically averaged) tide as shown in Figs. 6 and 7. The magnitude of the surface manifestation of the internal tide is approximately $\Delta\rho/\rho_0$ times η_0 ($\sim 10^{-3}$) (LeBlond and Mysak 1978; Apel 1987). The propagation of internal waves with a dominant wavelength appears clearly in Figs. 6 and 7. This result also indicates that the surface manifestation, associated with internal tide propagation, can be reasonably well represented in terms of a two-layer system, even though this representation is fairly schematic.

c. Tidal current ellipses

Tidal current ellipses are presented in Fig. 8 for the two-layer-averaged (barotropic) velocity ($u_{\rm bt}$, $v_{\rm bt}$)

$$u_{\rm bt} = \frac{U_1 + U_0}{h_1 + h_0}, \qquad v_{\rm bt} = \frac{V_1 + V_0}{h_1 + h_0}, \tag{9}$$

and in Fig. 9 for the upper-layer velocity (u_1, v_1). The upper-layer current (u_1, v_1) consists of the barotopic and baroclinic (u_{1bc}, v_{1bc}) components,

$$u_1 = u_{\rm bt} + u_{\rm 1bc}, \qquad v_1 = v_{\rm bt} + v_{\rm 1bc}. \tag{10}$$

The barotropic tidal currents in Fig. 8 are almost uniform, with counterclockwise rotation and small speeds of 2–3 cm s^{-1}, which agree with previously reported results (Luyten and Stommel 1991). Larger currents appear around the Hawaiian submarine ridge, probably due to a current flowing over the ridge at nearly a right angle. (The straight lines in the ellipses denote the current vector position at the time when the tide-generating body passes through Greenwich.) In addition, rectilinear tidal ellipses appear at lower latitudes.

Tidal ellipses in the upper layer (Fig. 9) display irregular features, indicating the strong influence of a baroclinic component, with current speeds larger than in

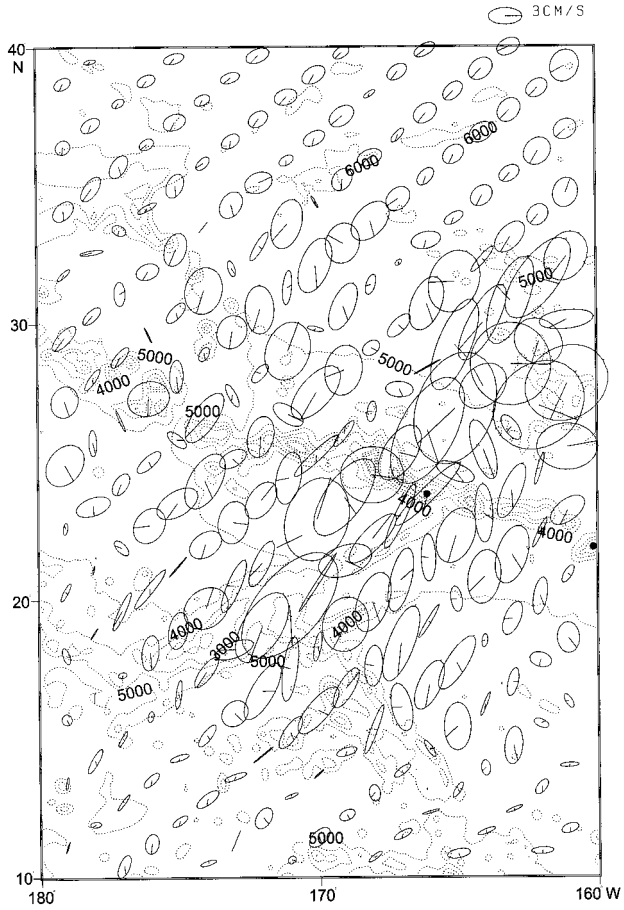

FIG. 9. The M_2 upper-layer current ellipses from RUN2, with an upper-layer thickness of 400 m. Current speeds are stronger than those of the barotropic current. Spatial variability in current speed prevails and the area of strong current coincides with the beam of internal waves shown in Figs. 5 and 11.

the barotropic ellipses. In many locations, the tidal current in the upper layer exceeds the barotropic current by a factor of 3–4. The maximum major-axis speed in Fig. 9 is about 10 cm s^{-1}. The nonuniformity of the tidal currents in Fig. 9 seems to reflect the ray path propagation of the internal tidal energy flux. This will be examined in section 3d.

Luyten and Stommel (1991) compared the observed M_2 tidal currents at 315 deep-sea locations with those computed by the numerical model of Schwiderski (1979). Such comparison is also made here and presented in Table 2. The current observed above Horizon Guyot by Noble et al. (1988) is also included in the comparison.

Our model barotropic currents show a somewhat better agreement with the Luyten and Stommel (1991) observations than do Schwiderski's values. However, Dushaw et al. (1997), through comparison of the current data and TPX0.2 global tide model (Egbert et al. 1994), showed that considerable scatter is evident in the current-meter values for the North Pacific and North Atlantic. That is, Dushaw et al. (1997) suggest that the current-meter data presented by Luyten and Stommel suffer from considerable random noise, arising from the motion of the current-meter mooring (Hendry 1977), or contamination by the baroclinic component (Luyten and Stommel 1991). In contrast to other observations, the observed current speed above Horizon Guyot is noticeably stronger than the barotropic model result. However, the computed current speeds in the upper layer do compare well in magnitude, even though there is about 50° deviation in the inclination angle. Noble et al. (1988) rejected the likelihood that these large currents arise from internal tides propagating from afar, suggesting instead that they were generated locally. On the other hand, the Ray and Mitchum (1996) TOPEX/Poseidon observations show strong southward propagation throughout this region. The present study also shows that internal tides generated over the Hawaiian Ridge propagate over the Horizon Guyot and that the baroclinic component plays a dominant role in enhancing current speeds there.

d. Barotropic and baroclinic energy fluxes

Using analyzed harmonics of the surface and interfacial disturbances and of the barotropic and baroclinic

TABLE 2. Comparison of the M_2 tidal current harmonics in the North Pacific. Data are taken from Luyten and Stommel (1991)(LS) and Noble et al. (1988)(NCS). Velocity (u, v) is in centimeters per second and phase lag (g_u, g_v) in degrees. Symbols a and b are the major- and minor-axis speeds of the tidal ellipses. θ is the orientation of the ellipse measured counterclockwise from the east, γ is the rotation, either clockwise (CW) or counterclockwise (CC).

Data source	Lat (deg)	Long (deg)	Depth (m)	Observed				Schwiderski				Model (barotropic)			
				u	g_u	v	g_v	u	g_u	v	g_v	u	g_u	v	g_v
LS	31.0	184.9	3993	1.7	247	1.2	197	1.1	265	1.3	200	1.4	24	1.4	183
LS	31.0	184.9	3996	1.8	265	1.2	219	1.1	265	1.3	200	1.4	240	1.4	183
LS	35.0	185.1	4006	1.4	313	1.5	237	1.2	258	1.2	198	1.4	228	1.3	175
				Observed current				Model (barotropic)				Model (upper layer)			
				a	b	θ	γ	a	b	θ	γ	a	b	θ	γ
NCS	19.5	191.3	213	7.6	3.1	142	CC	2.5	1.9	87	CW	4.4	4.0	92	CW

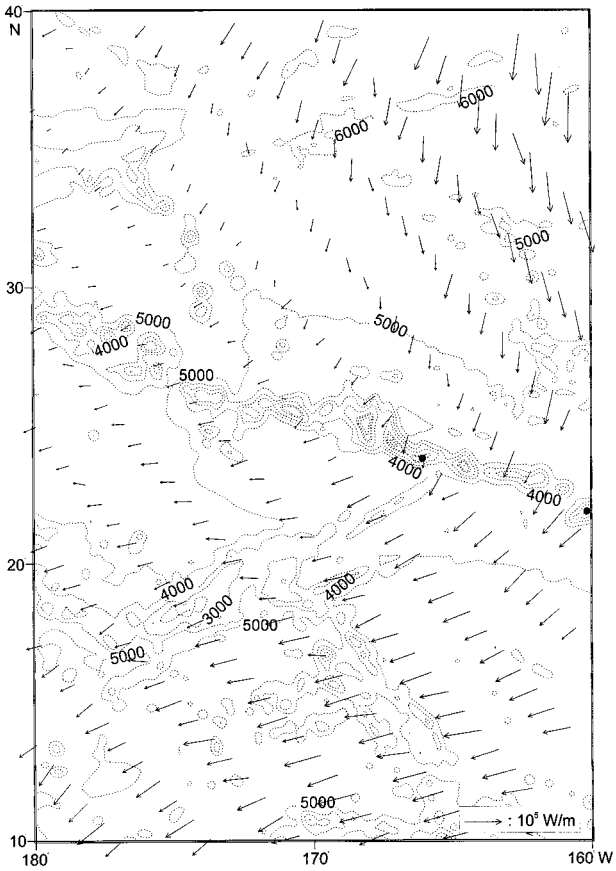

FIG. 10. Computed M_2 barotropic energy flux vectors from experiment RUN2. The barotropic energy flows from north-northeast to the south-southwest. Somewhat weaker energy flux densities appear around the ridge.

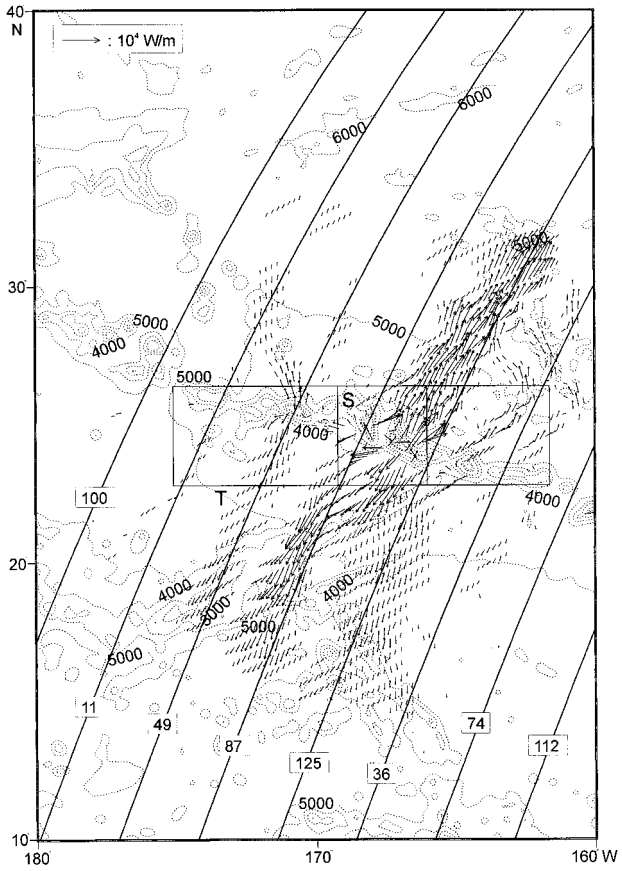

FIG. 11. Baroclinic M_2 energy flux vectors from experiment RUN2. Integrated energy fluxes are computed for rectangular regions S (S1–S4 are shown in Fig. 2) and T, in order to estimate the energy conversion from barotropic to first baroclinic mode from multiple energy source regions.

currents, time-averaged barotropic and baroclinic energy fluxes for the two-layer system (see appendix B) have been computed for the ninth cycle model result. The corresponding energy flux vectors are presented in Figs. 10 and 11.

Figure 10 shows that the barotropic energy flux is from north-northeast to west-southwest in the direction of the M_2 tide. The barotropic energy flux shows relatively large variability with values of about 100 kW m^{-1} in the northeast region, and nearly an order of magnitude less (10 kW m^{-1}) in the central region. The smaller magnitude in the central northwestern region is due to the smaller elevation amplitudes of 5–10 cm, as shown in the coamplitude charts (Figs. 3 and 4). The general features in Fig. 10 agree well with the barotropic tidal energy flux vectors shown by Ray and Mitchum (1997). It is worth noting that the barotropic energy fluxes appear to have some irregularity in their magnitude and direction. This spatial variability probably arises from baroclinic influences. It should not arise from diffraction effects since the modeled domain is located too far from Hawaiian Islands, as evident from the result of Larsen (1977). The irregular feature, especially in the amplitude, appears even farther to the southwest, down to 10°–15°N.

Figure 11 superimposes views of the baroclinic energy flux (see appendix B) on bathymetry. The baroclinic energy flux vectors are selectively presented at every tenth-grid interval. Only those of magnitude greater than 1 kW m^{-1} are displayed. The baroclinic energy flux is clearly seen to emanate from the Hawaiian Ridge toward the northeast and southwest in a horizontal beamlike pattern. A strongly radiating baroclinic energy flux in both directions can also be inferred from the fact that the bottom slopes (α) on the southern and northern banks of the crescent-shaped topography region (Fig. 2) of the ridge are larger than the internal tide characteristic slope

$$\tan\beta = \{(\omega^2 - f^2)/(N^2 - \omega^2)\}^{1/2}, \qquad (11)$$

where ω is the tidal frequency and $N = (g'/H_1)^{1/2}$ is the buoyancy frequency for a layered system (Richardson 1994), with parameter values taken for the RUN2 case and for latitude 24°N. According to the Baines (1974, 1982) theory, the generated internal tides are expected to radiate toward the deep waters (to the southwest and

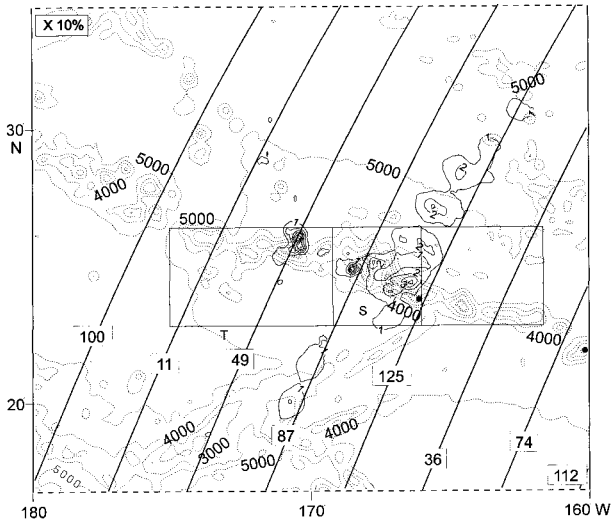

FIG. 12. Ratio of baroclinic to barotropic energy flux density. Except for two localized peaks, a high ratio region of 10%–40% appears between tracks of 125 and 87.

northeast) since the bottom slopes are supercritical ($\alpha > \tan\beta$). Also note that the direction of the baroclinic energy flux corresponds to the propagation direction of the interfacial disturbances, clearly seen in Fig. 5d.

It is worth noting the diverging or asymmetric energy flux pattern in low latitudes, along tracks 87 and 125. A similar feature also appears in the model results, Figs. 5c and 5d. The depth contours south of the ocean ridge region **S** do not show any abrupt changes. Considering that the agreement between the model results of Fig. 6a and the observed TOPEX/Poseidon results is reasonable along the southern part of track lines 125 and 87, the diverging or asymmetric pattern of the baroclinic energy beam (Fig. 11), or the propagation of interfacial waves (Figs. 5c and 5d), must be real. However, a dynamical explanation for this divergence is not obvious.

The intensity of the generated baroclinic tide is noticeably larger around the crescent-shaped topography (inside the region **S** in Figs. 2 and 11), with a peak flux density of 12.9 kW m^{-1}. This could be due to a superposition, or interference, away from a line source. In order to estimate the spatial distribution of the generated baroclinic flux, relative to the barotropic flux density, the ratio of baroclinic to barotropic energy flux density was calculated from the model results and the contours of equal percentage shown in Fig. 12. Ratio values are larger near the Hawaiian Ridge and values are in the range of 10%–40% near the region of crescent-shaped bottom topography (Fig. 2) around the ridge between tracks 125 and 87. Two locations showing values greater than 50% seem to be partly due to the relatively small barotropic energy flux, as seen in Fig. 12. The intensified baroclinic energy flux between tracks 125 and 87 is thought to appear because the crescent-shaped bottom topography feature focuses the baroclinic energy flux. It is also interesting to note that the ratios of baroclinic to barotropic energy flux fluctuate from 10% to 20(30)% in the northeastward direction. The distance between the fluctuating peaks is nearly equal to one internal tide wavelength of 150 km, and the locations of the peak value is nearly at the crests of the internal tidal waves in Fig. 5d.

TABLE 3. Integrated mean baroclinic and barotropic M_2 energy fluxes (GW) across the four sections in the western Hawaiian Ridge (Fig. 1). Positive (negative) flux values refer to northward (southward) or eastward (westward) directions.

Section	Baroclinic energy flux	Barotropic flux
S1	0.448	−8.622
S2	0.706	−11.032
S3	−0.894	−4.446
S4	−0.376	−12.568

In order to quantify the energy balance, both the baroclinic and barotropic components of the energy flux in region **S** (Figs. 2 and 11) are presented in Table 3. The integrated energy flux values are computed across four different sections: northern section (section **S**1), eastern section (section **S**2), southern section (section **S**3), and western section (section **S**4). Table 3 shows that the integrated barotropic M_2 energy flux across each section is about 5–20 times larger than the integrated M_2 baroclinic energy flux. The integrated baroclinic energy flux in a northeastern direction (sum of **S**1 and **S**2) is 1.15 GW, while this integrated energy flux in a southwestern direction (sum of **S**3 and **S**4) is 1.27 GW. The total integrated baroclinic M_2 energy flux emanating from the region **S** is therefore 2.42 GW. It is clear that energy flux emanating from any other energy region is much smaller than that from the box region. The total integrated baroclinic energy flux from the rectangular region **T** is 3.77 GW. Average northward, or southward, flux density is about 1.35 kW m^{-1} in the **T** region. The present model domain does not include the eastern Hawaiian Islands (reaching to 155°W). But, if we take 2.7 kW m^{-1} (1.35 kW m^{-1} to each side) for the whole 2000-km-long Hawaiian Ridge, we obtain a total baroclinic energy flux of 5.4 GW. Using both models and observations, Morozov (1995) estimated the M_2 energy flux values, transferred into internal tidal motion, for several World Ocean ridges and obtained 8 GW for the Hawaiian Ridge. Using simple parameters for a two-layered ocean. Ray and Mitchum (1997) estimated the mean integrated energy flux into phase-locked, first mode, baroclinic tide at the Hawaiian Ridge to be 15 GW. This translates to a mean flux of 4 kW m^{-1} for each of the northward and southward directions along this 2000-km-long ridge.

The agreement between the present result of 3.77 GW at western Hawaiian Ridge (5.4 GW if the whole 2000-km-long Hawaiian Ridge is considered) and the estimates of Morozov (1995) and Ray and Mitchum (1997) is not unreasonable, considering the approximate parameter values in their estimates and possible errors in

the present calculation. These results aslo indicate that there is a large uncertainty in the value of energy dissipation around the Hawaiian Ridge. [The Munk (1997) estimate of 0.2 TW for the global M_2 dissipation via internal tide conversion may require between 14 and 37 Hawaiian Ridges.]

The barotropic energy flux propagates from the north-northeast to south-southwest in model region **S**, resulting in negative energy flux values in Table 3. The loss of barotropic energy flux over this box region is calculated by summing the incoming integrated energy flux (sum of **S**1 and **S**2) and subtracting the outgoing integrated energy flux (sum of **S**3 and **S**4). This gives a loss of barotropic energy flux in the box region of 2.64 GW. The dissipation (d) in the turbulent bottom boundary layer (BBL) was calculated, following Taylor (1919) and Munk (1997):

$$d = C_d \overline{\rho} \langle U_s^3 \rangle \quad \text{W m}^{-2}, \tag{12}$$

where $C_d = 0.0025$, $\overline{\rho}$ is mean density and

$$U_s = \sqrt{u^2 + v^2}.$$

Averaging over one M_2 period and integrating over the region **S** yields $d = 0.029$ GW. This small amount of bottom dissipation in the ocean ridge region **S** seems to reflect the Munk (1997) remark that 99% of the ocean are accounts for less than 1% of the dissipation. Eventually, the loss of barotropic energy (2.64 GW) compares well with the sum (2.45 GW) of 0.029 GW of bottom boundary layer dissipation and 2.42 GW of integrated M_2 baroclinic energy flux leaving the region.

At this stage, it should be mentioned that numerical simulation of the baroclinic energy flux can be sensitive to errors in topography, the barotropic open boundary conditions, and also the choice of coefficients for bottom and interfacial dissipation. In addition, this two-layer model has limited application because the topographic features must be below the interfacial depth and shallow ridges must be smoothed out, both of which may cause errors in the intensity and radiated direction of baroclinic energy flux.

4. Summary

The generation, propagation, and surface manifestation of M_2 internal tides near the Hawaiian Ridge have been examined with a two-layer numerical model. This study confirms that the internal tide is generated by barotropic forcing at the Hawaiian Ridge and propagates in north-northeast and south-southwest directions. These results confirm the Dushaw et al. (1995) hypothesis and Ray and Mitchum (1996) analysis. The computed pattern of internal tidal waves between T/P tracks 87 and 125 suggests that the internal tides are generated at several regions along the Hawaiian Ridge, and form an interference pattern away from the ridge.

The surface manifestation of the M_2 simulated internal tide compares well with values resulting from the analysis of Topex/Poseidon satellite altimetry. The phase lag pattern of the internal waves reveals a wavelength of about 150 km and has in-phase and out-of-phase interactions with the background barotropic tidal waves. This phase-locked internal tide signal results in fluctuating amplitudes for the observed surface tide. The present model results and previous observations reveal that the surface manifestation of M_2 internal tide generation and propagation in the North Pacific can be reasonably well represented in terms of a simple two-layer system that can resolve the barotropic and first baroclinic modes.

Due to the presence of internal tides, the M_2 current ellipses in the upper ocean are dominated by the baroclinic component and exhibit large spatial variability in their magnitude relative to the barotropic tidal ellipses. This is also seen in the coastal area of British Columbia (Crawford et al. 1998). The internal tide generated over the Hawaiian Ridge propagates over Horizon Guyot, where Noble et al. (1988) observed M_2 current speeds stronger than expected from barotropic models.

Considerable spatial variability in the flux density of the first baroclinic mode was found in the baroclinic energy flux emanating from the western Hawaiian Ridge. A horizontal beamlike propagation from multiple sources was seen. Ratios of baroclinic to barotropic energy flux density are in the range of 10%–40% near the crescent-shaped bottom topography, between tracks 125 and 87. We estimate that about 3.8 GW of M_2 tidal power is converted from barotropic into first-mode baroclinic motion along the western ridge. With flux density of 2.7 kW m^{-1} (1.35 kW m^{-1} to each side) a total of 5.4 GW is converted from barotropic to baroclinic mode, for the 2000-km-long Hawaiian Ridge. Considering the uncertain parameters used in Morozov (1995) and Ray and Mitchum (1997), as well as various possible errors in the present calculation, the agreement between these estimates is reasonable. However, this study indicates that there is still a large uncertainty in the amount of energy converted from barotropic to radiating baroclinic tide at the Hawaiian Ridge.

Acknowledgments. The first author (S. K. Kang) acknowledges support from the Canadian Department of Fisheries and Oceans, the Canadian Panel for Energy Research and Development (PERD Project 24110), the Korea Science and Engineering Foundation (KOSEF), and Korea Ocean Research & Development Institute (PE99774) throughout this project. He is also grateful to C. Garrett of University of Victoria for his deep interest and discussion during S. K. Kang's visit to UVIC. We thank Dr. Claire Smith for a proof reading and two reviewers for constructive suggestions and valuable comments.

APPENDIX A

Discrete Approximation of Two-Layer System

A description of the numerical method used to solve the 1D governing equations is given in detail in Abbott (1979). Hodgins (1979), and Kang (1986, unpublished manuscript). Four component equations (continuity and momentum equations for the upper and lower layers) are solved interactively. The equations are discretized on an Arakawa C grid with a time- and space-centered scheme. In contrast to the one-dimensional case, the four component equations in x-direction sweep are first solved in two-dimensional space. That is, the continuity equations for the upper and lower layers and the x-direction momentum equations for the upper and lower layers are solved together. Surface and interfacial disturbances are centered over time step $(n + ½)$, while mass flux terms for the upper and lower layers are updated to $(n + 1)$. The four linear finite difference equations for the x direction are given as follows:

$$\frac{U_{1i,j}^{n+1} - U_{1,i,j}^{n}}{\Delta t} + \frac{gh_1}{R\cos\phi_{i,j}}\frac{h_{1i+1,j}^{n+1/2} - h_{1i-1,j}^{n+1/2}}{\Delta x} + \frac{gh_1}{R\cos\phi_{i,j}}\frac{ho_{i+1,j}^{n+1/2} - ho_{i-1,j}^{n+1/2}}{\Delta x} + \frac{gh_1}{R\cos\phi_{i,j}}\frac{Z_{i+1,j} - Z_{i-1,j}}{\Delta x}$$
$$= \frac{1}{2}\frac{K_i}{\Delta z}\left(\frac{U_{1i,j}^{n+1}}{h_{1i,j}^{n}} - \frac{Uo_{i,j}^{n+1}}{ho_{i,j}^{n}}\right) + \frac{1}{2}\frac{K_i}{\Delta z}\left(\frac{U_{1i,j}^{n}}{h_{1i,j}^{n}} - \frac{Uo_{i,j}^{n}}{ho_{i,j}^{n}}\right) + 2\omega\sin\phi\overline{V_{1i,j}^{n+1}} \tag{A1}$$

$$R\cos\phi_{i,j}\frac{h_{1i,j}^{n+1/2} - h_{1i,j}^{n}}{\Delta t} + \left\{\frac{1}{2}\frac{U_{1i+1,j}^{n+1} - U_{1i-1,j}^{n+1}}{\Delta x} + \frac{1}{2}\frac{U_{1i+1,j}^{n} - U_{1i-1,j}^{n}}{\Delta x}\right\}$$
$$+ \left\{\frac{1}{2}\frac{V_{1i+1,j}^{n+1/2}\cos\phi_{i,j+1} - V_{1i-1,j}^{n+1/2}\cos\phi_{i,j-1}}{\Delta\phi} + \frac{1}{2}\frac{V_{1i+1,j}^{n-1/2}\cos\phi_{i,j+1} - V_{1i-1,j}^{n-1/2}\cos\phi_{i,j-1}}{\Delta\phi}\right\}$$
$$= 0 \tag{A2}$$

$$\frac{Uo_{i,j}^{n+1} - Uo_{i,j}^{n}}{\Delta t} + \frac{gh_0}{R\cos\phi_{i,j}}\frac{ho_{i+1,j}^{n+1/2} - ho_{i-1,j}^{n+1/2}}{\Delta x} + \frac{\lambda gh_0}{R\cos\phi_{i,j}}\frac{h_{1i+1,j}^{n+1/2} - h_{1i-1,j}^{n+1/2}}{\Delta x} + \frac{gh_0}{R\cos\phi_{i,j}}\frac{Z_{i+1,j} - Z_{i-1,j}}{\Delta x}$$
$$= \frac{1}{2}\frac{K_i}{\Delta z}\left(\frac{U_{1i,j}^{n+1}}{h_{1i,j}^{n}} - \frac{Uo_{i,j}^{n+1}}{ho_{i,j}^{n}}\right) + \frac{1}{2}\frac{K_i}{\Delta z}\left(\frac{U_{1i,j}^{n}}{h_{1i,j}^{n}} - \frac{Uo_{i,j}^{n}}{ho_{i,j}^{n}}\right) + 2\omega\sin\phi\overline{Vo_{i,j}^{n+1}} \tag{A3}$$

$$R\cos\phi_{i,j}\frac{ho_{i,j}^{n+1/2} - ho_{i,j}^{n}}{\Delta t} + \left\{\frac{1}{2}\frac{Uo_{i+1,j}^{n+1} - Uo_{i-1,j}^{n+1}}{\Delta x} + \frac{1}{2}\frac{Uo_{i+1,j}^{n} - Uo_{i-1,j}^{n}}{\Delta x}\right\}$$
$$+ \left\{\frac{1}{2}\frac{Vo_{i+1,j}^{n+1/2}\cos\phi_{i,j+1} - Vo_{i-1,j}^{n+1/2}\cos\phi_{i,j-1}}{\Delta\phi} + \frac{1}{2}\frac{Vo_{i+1,j}^{n-1/2}\cos\phi_{i,j+1} - Vo_{i-1,j}^{n-1/2}\cos\phi_{i,j-1}}{\Delta\phi}\right\}$$
$$= 0, \tag{A4}$$

where an overbar denotes the spatial average at a given point (i, j). In a y-direction sweep, another four equations for the y momentum equations and continuity equations for the lower and upper layers are solved simultaneously. The surface and interfacial disturbances are updated from $(n + ½)$ to $(n + 1)$ and the y component of mass flux from (n) to $(n + 1)$. Therefore, eight component equations are solved together. Each of the finite difference equations requires a penta-diagonal matrix equation to be solved as follows, subject to boundary conditions from both boundaries.

$$A_{i,j}h_{1j-1} + B_{i,j}ho_{j-1} + C_{i,j}U_{1j} + D_{i,j}Uo_j + E_{i,j}h_{1j+1} + F_{i,j}ho_{j+1} = G_{i,j}. \tag{A5}$$

Here $i = 1, 2, 3, 4$ denotes difference equations corresponding to continuity equations for the upper and lower layers and momentum equations for the upper and lower layers, respectively, and j is a given y or x grid point.

The algebraic relation for the scalar form solution of the equation system (A5) is described in Kang (1986). The nonlinear and the horizontal diffusion terms are also discretized in space and time with a centered difference scheme, and the nonlinear terms are solved in terms of special side feeding technique.

In relation to boundary conditions, there are five distinct characteristic structures in the two-layer stratified fluid case. This was described in detail in Abbott (1979). The number of data points presented at each boundary

equals the number of characteristics initiated from any point on the boundary and heading forward in time. In the present experiment of internal tide modeling, the flow is considered only for subcritical flow in both layers. An initial computation requires each two-point boundary data in each *x*- and *y*-direction computation. The tidal variations are given as lower-layer values, while the thickness of the upper layer is given for the boundary value of the upper layer.

APPENDIX B

Energetics of Two-Layer System

The energy equation for linear two-layered flow, without forcing and dissipation terms, is given as (LeBlond and Mysak 1978), with subscript 0 for lower layer,

$$\frac{\partial}{\partial t}\left[\frac{1}{2}\rho_1(u_1^2 + v_1^2) + \frac{1}{2}\rho_0(u_0^2 + v_0^2)\right] + \frac{\partial}{\partial t}\left[\frac{1}{2H_1}\rho_1 g\eta_1^2 + \frac{1}{2H_0}\rho_0 g'\eta_0^2\right] + \left[\rho_1 g\frac{H_1 - H_0}{H_1 H_0}\eta_1\frac{\partial \eta_0}{\partial t}\right] + g\nabla\cdot[\rho_1\mathbf{u}_1 + \rho_0\mathbf{u}_0)\eta_1] + \rho_0 g'\nabla\cdot[\mathbf{u}_0(\eta_0 - \eta_1)] = 0. \quad \text{(B1)}$$

Here g' is the reduced gravity for a two layer fluid. The first square-bracketed term represents the (time) rate of change of the kinetic energy in the two layers: the second, the rate of change of potential energy for the surface and interfacial displacements: the third, an interaction term between the surface and interfacial disturbance: the last two terms, the divergence of the energy fluxes in the two layers. Alternatively, the layer-integrated form of the energy equation can be written as follows:

$$\frac{\partial}{\partial t}\left[\frac{1}{2}\rho_1 H_1(u_1^2 + v_1^2) + \frac{1}{2}\rho_0 H_0(u_0^2 + v_0^2)\right] + \frac{\partial}{\partial t}\left[\frac{1}{2}\rho_1 g\eta_1^2 + \frac{1}{2}\rho_0 g'\eta_0^2\right] + \nabla\cdot(J_1 + J_2) + \nabla\cdot J_3 = 0, \quad \text{(B2)}$$

where

$$J_1(x, y) = g\rho_1 H_1(u_1, v_1)\eta_1,$$
$$J_2(x, y) = g\rho_0 H_0(u_0, v_0)\eta_1,$$
$$J_3(x, y) = \rho_0 g' H_0(\eta_0 - \eta_1)(u_0, v_0) \quad \text{(B3)}$$

[J_1, J_2, and J_3 represent the energy flux (in W m^{-1})]. The barotropic (bt) and baroclinic (bc) energy flux can be calculated as follows. The current in each layer consists of barotropic and baroclinic components. The barotropic (two-layer averaged) current $\mathbf{u}_{bt}(u_{bt}, v_{bt})$ is defined in Eq. (9) using mass fluxes and thickness of the upper and lower layers.

The velocity consists of the barotropic component and the baroclinic component for the upper layer, $\mathbf{u}_{1bc}(u_{1bc}, v_{1bc})$, and for the lower layer, $\mathbf{u}_{0bc}(u_{0bc}, v_{0bc})$, as follows:

$$u_1 = u_{bt} + u_{1bc} \qquad u_0 = u_{bt} + u_{0bc}. \quad \text{(B4)}$$

The relation for the total mass flux of the baroclinic mode is

$$H_1 u_{1bc} + H_0 u_{0bc} = 0. \quad \text{(B5)}$$

Then, the *x* component of the energy flux is

$$\begin{aligned}(J_1 + J_2 + J_3)_x &= g\rho_1 H_1 u_1\eta_1 + g\rho_0 H_0 u_0\eta_1 + \rho_0 g' H_0(\eta_0 - \eta_1)u_0 \\ &= g u_{bt}\eta_1\rho_1(H_1 + H_0) + \rho_1 g\eta_1(H_1 u_{1bc} + H_0 u_{0bc}) \\ &\quad + \rho_0 g' H_0\eta_0 u_{0bc} + (\rho_0 - \rho_1)gH_0\eta_0 u_{bt} \\ &= \rho_1 gH\eta_1 u_{bt} + (\rho_0 - \rho_1)gH_0\eta_0 u_{0bc} \\ &\quad + (\rho_0 - \rho_1)gH_0\eta_0 u_{bt}. \end{aligned} \quad \text{(B6)}$$

Similarly, the *y* component of velocity is

$$v_1 = v_{bt} + v_{1bc} \qquad v_0 = v_{bt} + v_{0obc}, \quad \text{(B7)}$$

and the relation for zero mass flux of baroclinic mode in *y* direction is

$$H_1 v_{1bc} + H_0 v_{0bc} = 0. \quad \text{(B8)}$$

Then *y* component of energy flux is

$$(J_1 + J_2 + J_3)_y = \rho_1 gH\eta_1 v_{bt} + (\rho_0 - \rho_1)gH_0\eta_0 v_{0bc} + (\rho_0 - \rho_1)gH_0\eta_0 v_{bt}. \quad \text{(B9)}$$

An average of energy fluxes over one tidal period yields the time-averaged barotropic energy flux ($\mathbf{J}_{bt}$) and the time-averaged baroclinic energy flux ($\mathbf{J}_{bc}$), as

$$\mathbf{J}_{bt} = \left(\frac{1}{2}\rho_1 g\widehat{u_{bt}}\widehat{\eta_1}\cos(\theta_{\eta 1} - \theta_{ubt}), \frac{1}{2}\rho_1 g\widehat{v_{bt}}\widehat{\eta_1}\cos(\theta_{\eta 1} - \theta_{vbt})\right). \quad \text{(B10)}$$

$$\mathbf{J}_{bc} = \left(\frac{1}{2}(\rho_0 - \rho_1)g\widehat{u_{0bc}}\widehat{\eta_0}\cos(\theta_{\eta 0} - \theta_{u0bc}), \frac{1}{2}(\rho_0 - \rho_1)g\widehat{v_{0bc}}\widehat{\eta_0}\cos(\theta_{\eta 0} - \theta_{v0bc})\right), \quad \text{(B11)}$$

where $(\hat{u}_{bt}, \hat{v}_{bt})$ is the *x*, *y* amplitude of barotropic current: θ_{ubt} is the phase lag of the *x* component of barotropic current: θ_{vbt} is the phase lag of *y* component of barotropic current: $(\hat{\eta}_1, \theta_{\eta 1})$ are the amplitude and phase lag of surface disturbance: $(\hat{\eta}_0, \theta_{\eta 0})$ are the amplitude and phase lag of interfacial disturbance: $(\hat{u}_{0bc}, \hat{v}_{0bc})$ are the *x*- and *y*-amplitudes of baroclinic current in the lower layer: $(\theta_{0bc}, \theta_{0bc})$ are the *x*- and *y*-phase lags of baro-

clinic current in the lower layer. These amplitudes and phase lags are obtained by harmonic analysis of currents and of surface and interfacial disturbances.

REFERENCES

Abbott, M. B., 1979: *Computational Hydraulics: Elements of the Theory of Free Surface Flows.* Longman, 326 pp.

——, and D. R. Basco, 1989: *Computational Fluid Dynamics: An Introduction for Engineers.* John Wiley and Sons, 425 pp.

——, A. McCowan, and I. R. Warren, 1981: Numerical modeling of free-surface flows and coastal waters. *Transport Models for Inland and Coastal Waters,* H. B. Fisher, Ed., Academic Press, 542 pp.

Apel, J. R., 1987: *Principles of Ocean Physics.* Academic Press, 634 pp.

Baines, P. G., 1974: The generation of internal tides over steep continental slopes. *Philos. Trans. Roy. Soc. London,* **A277,** 27–58.

——, 1982: On internal tide generation models. *Deep-Sea Res.,* **29,** 307–338.

Chiswell, S. M., 1994: Vertical structure of the baroclinic tides in the central North Pacific subtropical gyre. *J. Phys. Oceanogr.,* **24,** 2032–2039.

Crawford, W. R., J. Y. Cherniawsky, P. F. Cummins, and M. G. G. Foreman, 1998: Variability of tidal currents in a wide strait: A comparison between drifter observations and numerical simulation. *J. Geophys. Res.,* **103** (C6), 12 743–12 759.

Cummins, P. F., and L. Y. Oey, 1997: Simulation of barotropic and baroclinic tides off northern British Columbia. *J. Phys. Oceanogr.,* **27,** 762–781.

Deardorff, J. W., 1971: On the magnitude of the subgrid scale eddy coefficient. *J. Comput. Phys.,* **7,** 120–133.

Dushaw, B. D., and P. F. Worcester, 1998: Resonant diurnal internal tides in the North Atlantic. *Geophys. Res. Lett.,* **25,** 2189–2192.

——, B. D. Cornuelle, P. F. Worcester, B. M. Howe, and D. S. Luther, 1995: Barotropic and baroclinic tides in the central North Pacific ocean determined from long-range reciprocal acoustic transmissions. *J. Phys. Oceanogr.,* **25,** 631–647.

——, G. D. Egbert, P. F. Worcester, B. D. Cornuelle, B. M. Howe, and K. Metzger, 1997: A TOPEX/Poseidon global tidal model (TPX0.2) and barotropic tidal currents determined from long-range acoustic transmissions. *Progress in Oceanography,* Vol. 40, Pergamon, 337–367.

Egbert, G. D., A. F. Bennett, and M. G. G. Foreman, 1994: TOPEX/POSEIDON tides estimated using a global inverse model. *J. Geophys. Res.,* **99,** 24 821–24 852.

Gill, A. E., 1982: *Atmosphere–Ocean Dynamics.* Academic Press, 662 pp.

Hendry, R. M., 1977: Observations of the semidiurnal internal tide in the western North Atlantic Ocean. *Philos. Trans. Roy. Soc. London,* **A286,** 1–24.

Hodgins, D. O., 1979: On the numerical computation of two-layer nearly horizontal flows. *J. Hydraul. Res.,* **17,** 23–42.

Holloway, P. E., 1996: A numerical model of internal tides with application to the Australian North West Shelf. *J. Phys. Oceanogr.,* **26,** 21–37.

Irish, J., W. H. Munk, and F. Snodgrass, 1971: M_2 amphidrome in the northeast Pacific. *Geophys. Fluid Dyn.,* **2,** 355–360.

——, S. R. Lee, and H. J. Lie, 1998: Fine grid tidal modeling of the Yellow and East China Seas. *Contin. Shelf Res.,* **18,** 739–772.

Kang, S. K., 1986: Mathematical modeling of two-layer flow in one dimension. Internal Rep., IHE, Delft, Netherlands.

Karl, D. M., and R. Lukas, 1996: The Hawaiian Ocean Time-series (HOT) Program: Background, rationale and field implementation. *Deep-Sea Res., Part II,* **43,** 129–156.

Larsen, J. C., 1977: Cotidal charts for the Pacific Ocean near Hawaii using f-plane solution. *J. Phys. Oceanogr.,* **7,** 100–109.

LeBlond, P. H., 1966: On the damping of internal gravity waves in a continuously stratified ocean. *J. Fluid Mech.,* **25,** 121–142.

——, and L. A. Mysak, 1978: *Waves in the Ocean.* Elsevier, 602 pp.

LeProvost, C., A. F. Bennett, and D. E. Cartwright, 1995: Ocean tides for and from TOPEX/Poseidon. *Science,* **267,** 639–642.

Luyten, J. R., and H. M. Stommel, 1991: Comparison of M_2 tidal currents observed by some deep moored current meters with those of the Schwiderski and Laplace models. *Deep-Sea Res.,* **38** (Suppl.), S573–S589.

Morozov, E. G., 1995: Semidiurnal internal wave global field. *Deep-Sea Res.,* **42,** 135–148.

Munk, W. H., 1997: Once again: Once again—Tidal friction. *Progress in Oceanography,* Vol. 40, Pergamon, 7–35.

——, and C. Wunsch, 1998: Abyssal recipes II: Energetics of tidal and wind mixing. *Deep-Sea Res.,* **45,** 1977–2010.

Noble, M., D. A. Cacchione, and W. C. Schwab, 1988: Observation of strong mid-Pacific internal tides above Horizon Guyot. *J. Phys. Oceanogr.,* **18,** 1300–1306.

Pickard, G. L., 1979: *Descriptive Physical Oceanography.* Pergamon, 233 pp.

Pingree, R. D., and D. K. Griffiths, 1987: Tidal friction for semidiurnal tides. *Contin. Shelf Res.,* **7,** 1181–1209.

——, ——, and G. T. Mardell, 1983: The structure of the Celtic Sea shelf break. *J. Mar. Biol. Assoc. U.K.,* **64,** 99–113.

Ray, R. D., and G. T. Mitchum, 1996: Surface manifestation of internal tides generated near Hawaii. *Geophys. Res. Lett.,* **23,** 2101–2104.

——, and ——, 1997: Surface manifestation of internal tides in the deep ocean: Observation from altimetry and island gauges. *Progress in Oceanography,* Vol. 40, Pergamon, 135–162.

Richardson, L. F., 1994: Part IV: Combined rotation and stratification effects. *Introduction to Geophysical Fluid Dynamics,* B. Cushman-Roisin, Ed., Prentice-Hall, 320 pp.

Schrama, E. J. O., and R. D. Ray, 1994: A preliminary tidal analysis of TOPEX/Poseidon altimetry. *J. Geophys. Res.,* **99,** 24 799–24 808.

Schwiderski, E. W., 1979: Global ocean tides. Part II: The semidiurnal principal lunar tide M_2. Atlas of tidal charts and maps. Naval Surface Weapon Center Tech. Rep. TR 79-414, 87 pp.

Serpette, A., and R. Maze, 1989: Internal tides in the Bay of Biscay: A two-dimensional model. *Contin. Shelf Res.,* **9,** 795–821.

Smagorinsky, J. S., 1963: General circulation experiment with the primitive equations: I. The basic experiment. *Mon. Wea. Rev.,* **91,** 99–164.

Taylor, G. I., 1919: Tidal friction in the Irish Sea. *Philos. Trans. Roy. Soc. London,* **A220,** 1–93.

Tupas, L., F. Santiago-Mandujano, D. Hebel, E. Firing, R. Lukas, and D. Karl, 1995: 1994 Hawaii Ocean Time-series Program. Data Rep. SOEST 95–6, 199 pp. [Available from School of Ocean and Earth Science and Technology, University of Hawaii, 1680 East-West Rd., Honolulu, HI 96822.]

Willmott, A. J., and P. D. Edwards, 1987: A numerical model for the generation of tidally forced nonlinear internal waves over topography. *Contin. Shelf Res.,* **5,** 457–484.